

See discussions, stats, and author profiles for this publication at: <https://www.researchgate.net/publication/237315805>

# Thin films of block copolymer

ARTICLE *in* THE JOURNAL OF CHEMICAL PHYSICS · MAY 1997

Impact Factor: 2.95 · DOI: 10.1063/1.473778

---

CITATIONS

283

---

READS

67

## 1 AUTHOR:



Mark W Matsen

University of Waterloo

134 PUBLICATIONS 7,827 CITATIONS

SEE PROFILE

# Thin films of block copolymer

M. W. Matsen

*Polymer Science Centre, University of Reading, Whiteknights, Reading RG6 6AF, United Kingdom*

(Received 27 November 1996; accepted 4 February 1997)

We develop a numerical method for examining complex morphologies in thin films of block copolymer using self-consistent field theory. Applying the method to confined films of symmetric diblock copolymer, we evaluate the stability of parallel, perpendicular, and mixed lamellar phases. In general, lamellar domains formed by the diblocks are oriented parallel to the film by surface fields. However, their orientation can flip to perpendicular when the natural period of the lamellae is incommensurate with the film thickness. Experiments and Monte Carlo simulations have indicated that mixed lamellar phases may also occur, but for symmetric diblocks, we find these phases to be slightly unstable relative to perpendicular lamellae. Nevertheless, just a small asymmetry in the molecule stabilizes a mixed lamellar phase. Although our work focuses on confined films, we do discuss the behavior that results when films are unconfined. © 1997 American Institute of Physics. [S0021-9606(97)50718-5]

## I. INTRODUCTION

The study of block copolymer melts has progressed to the stage where bulk phase behavior is well understood. With this accomplishment in hand, researchers are well posed to tackle other more specialized behavior. One area that has drawn substantial interest recently is the study of block copolymer thin films,<sup>1</sup> partly because of their potential applications for coating surfaces. Not only is this research liable to yield important commercial uses for block copolymers, it provides a sensitive way of probing the competition between chain stretching and interfacial tension which controls the selection of ordered microstructures.<sup>2</sup> Furthermore, thin films appear to be an ideal system in which to study the effects of external fields on block copolymer morphology.<sup>3</sup>

Considerable progress towards the understanding of block copolymer films has already been achieved. The first experiments<sup>4-7</sup> examined unconfined films supported by a solid substrate, and focused on symmetric diblocks that in the bulk form a lamellar microstructure with some period  $D_b$ . Due to the air/polymer surface tension, flat films tend to develop with a uniform thickness  $\Delta$ . Usually, each surface of the film has a significant preferential affinity towards one of the polymer species, and this aligns lamellae with the film producing a parallel lamellar ( $L_\nu^\parallel$ ) phase. Ideally, the number of interfaces in the film  $\nu$  equals  $2\Delta/D_b$  allowing the lamellae to acquire their preferred thickness. However,  $\nu$  is restricted to either even integers if the two surfaces have an affinity for the same polymer species, or odd integers if the surfaces attract the opposite species. Thus a uniform film typically results in a frustrated domain spacing. To allow the spacing to relax to its natural size, the film phase separates into two thicknesses producing a terraced air/polymer surface.

More recent experiments<sup>8-10</sup> have dealt with confined films where both surfaces are hard walls preventing phase separation of the film thickness and producing a wider variety of ordering phenomena. In this case, frustration in the  $L_\nu^\parallel$  phase can be relieved if the parallel lamellae flip forming

a lamellar ( $L^\perp$ ) phase with layers perpendicular to the film<sup>8</sup> (see Fig. 1). Although such a phase has a less favorable surface energy, its period  $D$  is free to relax to the bulk spacing  $D_b$ . There are also experimental<sup>9</sup> and Monte Carlo<sup>11</sup> results showing that parallel lamellae can relax by forming a mixed lamellar ( $L_\nu^M$ ) phase with  $\nu$  parallel interfaces adjacent to one surface and perpendicular interfaces at the other surface (see Fig. 1). Although the boundary between the two orientations of lamellae costs energy, this is compensated by the lower surface energy with the parallel lamella. New experimental techniques,<sup>8</sup> that allow a continuous variation of the surface interactions, promise to provide systematic experimental studies of this system.

In this paper, we perform a theoretical study on thin films of diblock copolymer using self-consistent field theory (SCFT).<sup>12</sup> Previous calculations using SCFT (Ref. 13) have been restricted to phases without lateral structure (i.e.,  $L_\nu^\parallel$ ). Here we develop a numerical method for examining thin films with an arbitrary laterally periodic structure (i.e.,  $L^\perp$  and  $L_\nu^M$ ). Using this method, a phase diagram is calculated for confined films of symmetric diblock copolymer at an intermediate degree of segregation. Although the mixed lamellar phase is found to be slightly unstable, we show that a small degree of asymmetry in the molecule causes it to become stable. We also compare our results to strong-segregation theory (SST) (Ref. 14) and present some calculations for unconfined films.

## II. THEORY

We consider a melt of  $n$  AB diblock copolymers, where the A and B blocks consist of  $fN$  and  $(1-f)N$  segments, respectively. The melt is confined to a film of area  $\mathcal{A}$ , thickness  $\Delta_0$ , and volume  $\mathcal{V}_0 \equiv \Delta_0 \mathcal{A}$ . The segments are defined so that the bulk density of each species is  $\rho_0$ . In terms of this density, an effective volume  $\mathcal{V} \equiv nN/\rho_0$  can be defined and from that an effective thickness  $\Delta \equiv \mathcal{V}/\mathcal{A}$ . This is a more useful measure of the film thickness than  $\Delta_0$ . We assume that the A and B segments have the same statistical length

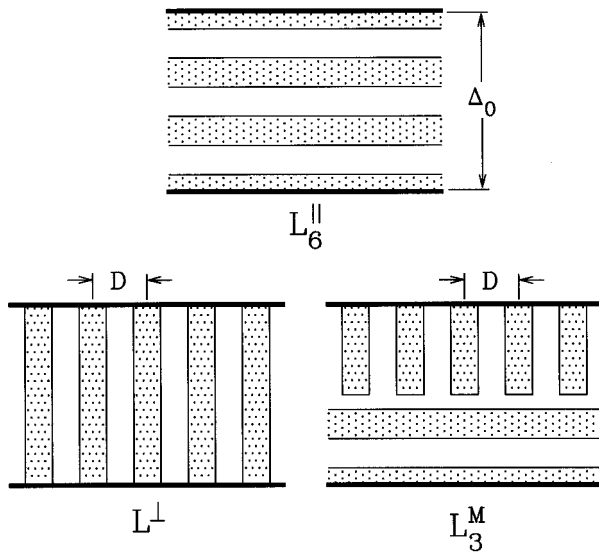


FIG. 1. Schematic illustrations of the A and B domains in the parallel ( $L_v^||$ ), perpendicular ( $L^\perp$ ), and mixed ( $L_3^M$ ) lamellar phases. The index  $v$  denotes the number of A/B interfaces parallel to the film. Bold lines represent hard walls separated by a distance  $\Delta_0$ . Below we define a more convenient measure of the film thickness  $\Delta$  based on the amount of polymer material, which is slightly smaller than  $\Delta_0$ . In the lower two illustrations,  $D$  represents the period of the lateral structure.

$a$ , but the generalization to distinct segment lengths is straightforward.<sup>15</sup> Each polymer is parameterized with a variable,  $s$ , that increases continuously along its length. Beginning at the A end of the diblock  $s=0$ , at the junction  $s=f$ , and at the B end  $s=1$ . Using this parameterization, the function,  $\mathbf{r}_\alpha(s)$ , is defined to specify the configuration of the  $\alpha$ 'th polymer.

In terms of the above definitions, a dimensionless operator for the A segment density is expressed as

$$\hat{\phi}_A(\mathbf{r}) = \frac{N}{\rho_0} \sum_{\alpha=1}^n \int_0^f ds \delta(\mathbf{r} - \mathbf{r}_\alpha(s)). \quad (1)$$

An analogous definition is made for the B segment density  $\hat{\phi}_B(\mathbf{r})$ . Generally, it is reasonable to assume that a polymer melt is incompressible and therefore enforce the constraint  $\hat{\phi}_A(\mathbf{r}) + \hat{\phi}_B(\mathbf{r}) = 1$ . However, the polymer concentration vanishes at a surface and so this constraint cannot be applied to the present system. Past works involving surfaces have allowed the melt to be compressible by including either a simple compressibility term in the Hamiltonian<sup>16</sup> or doing a more sophisticated equation-of-state treatment of the segment density.<sup>17</sup> Here the details regarding the segment profile at the two surfaces are not important, and so we take a simpler approach. We generalize the incompressibility constraint to  $\hat{\phi}_A(\mathbf{r}) + \hat{\phi}_B(\mathbf{r}) = \Phi_0(\mathbf{r})$  and choose

$$\Phi_0(\mathbf{r}) = \begin{cases} (1 - \cos(\pi x/\epsilon))/2, & \text{if } 0 \leq x \leq \epsilon, \\ 1, & \text{if } \epsilon \leq x \leq \Delta_0 - \epsilon, \\ (1 - \cos(\pi(\Delta_0 - x)/\epsilon))/2, & \text{if } \Delta_0 - \epsilon \leq x \leq \Delta_0. \end{cases} \quad (2)$$

This positions the film orthogonal to the  $x$ -direction between  $x=0$  and  $x=\Delta_0$ . The distance  $\epsilon$  from the wall over which the segment density rises to 1 should be selected much smaller than  $aN^{1/2}$ , the RMS end-to-end length of an unperturbed polymer molecule. If desired, the present calculation can be extended to treat the surface profile in a more realistic fashion as in Ref. 17.

Having specified the system, we now present the self-consistent field theory (SCFT) which describes it. Our derivation for block copolymer films closely parallels that for bulk melts.<sup>18</sup> To begin, the partition function is written as

$$Z = \int \left( \prod_{\alpha=1}^n \mathcal{D}\mathbf{r}_\alpha P[\mathbf{r}_\alpha; 0, 1] \right) \delta[\Phi_0 - \hat{\phi}_A - \hat{\phi}_B] \times \exp \left\{ -\rho_0 \int d\mathbf{r} [\chi \hat{\phi}_A(\mathbf{r}) \hat{\phi}_B(\mathbf{r}) - H(\mathbf{r})(\hat{\phi}_A(\mathbf{r}) - \hat{\phi}_B(\mathbf{r}))] \right\}, \quad (3)$$

where the functional integral is over all configurations of the system. We assume flexible Gaussian polymers, and therefore weight their individual configurations by the functional,<sup>12</sup>

$$P[\mathbf{r}_\alpha; s_1, s_2] \propto \exp \left\{ -\frac{3}{2Na^2} \int_{s_1}^{s_2} ds \left| \frac{d}{ds} \mathbf{r}_\alpha(s) \right|^2 \right\}. \quad (4)$$

The Flory-Huggins parameter,  $\chi$ , measures the incompatibility between A and B segments, and  $H(\mathbf{r})$  is a surface field. For the latter, we choose a convenient functional form,

$$H(\mathbf{r}) = \begin{cases} \Lambda_1(1 + \cos(\pi x/\epsilon))aN^{1/2}/\epsilon, & \text{if } 0 \leq x \leq \epsilon, \\ 0, & \text{if } \epsilon \leq x \leq \Delta_0 - \epsilon, \\ \Lambda_2(1 + \cos(\pi(\Delta_0 - x)/\epsilon))aN^{1/2}/\epsilon, & \text{if } \Delta_0 - \epsilon \leq x \leq \Delta_0, \end{cases} \quad (5)$$

where  $\Lambda_1$  controls the strength of the field at the  $x=0$  surface, and  $\Lambda_2$  does the same for the  $x=\Delta_0$  surface.

To make the expression for the partition function more tractable, we insert the integral  $\int \mathcal{D}\Phi_A \delta[\Phi_A - \hat{\phi}_A]$  permitting the replacement of  $\hat{\phi}_A$  in Eq. (3) by  $\Phi_A$ ; the same is done for the B segment distribution. Next the delta functionals are replaced by integral representations, which brings the partition function into the form

$$Z = \mathcal{N}^3 \int \mathcal{D}\Phi_A \mathcal{D}W_A \mathcal{D}\Phi_B \mathcal{D}W_B \mathcal{D}\Xi \times \exp \{ -F[\Phi_A, W_A, \Phi_B, W_B, \Xi]/k_B T \}, \quad (6)$$

with

$$\begin{aligned}
& F[\Phi_A, W_A, \Phi_B, W_B, \Xi]/nk_B T \\
& \equiv -\ln \mathcal{Q}[W_A, W_B] + \mathcal{N}^{-1} \int d\mathbf{r} [\chi N \Phi_A(\mathbf{r}) \Phi_B(\mathbf{r}) \\
& \quad - H(\mathbf{r}) N (\Phi_A(\mathbf{r}) - \Phi_B(\mathbf{r})) - W_A(\mathbf{r}) \Phi_A(\mathbf{r}) \\
& \quad - W_B(\mathbf{r}) \Phi_B(\mathbf{r}) - \Xi(\mathbf{r}) \\
& \quad \times (\Phi_0(\mathbf{r}) - \Phi_A(\mathbf{r}) - \Phi_B(\mathbf{r}))], \quad (7)
\end{aligned}$$

and

$$\begin{aligned}
\mathcal{Q}[W_A, W_B] \equiv \int \mathcal{D}\mathbf{r}_\alpha P[\mathbf{r}_\alpha; 0, 1] \exp \left\{ - \int_0^f ds W_A(\mathbf{r}_\alpha(s)) \right. \\
\left. - \int_f^1 ds W_B(\mathbf{r}_\alpha(s)) \right\}. \quad (8)
\end{aligned}$$

The last quantity,  $\mathcal{Q}[W_A, W_B]$ , is the partition function of a single non-interacting polymer in external fields,  $W_A(\mathbf{r})$  and  $W_B(\mathbf{r})$ . The above transformation is exact.

The functional,  $F[\Phi_A, W_A, \Phi_B, W_B, \Xi]$ , can be evaluated exactly, but the functional integral in Eq. (6) cannot. In the SCFT, the integral is approximated by the extremum of the integrand, and thus the free energy,  $-k_B T \ln Z$ , is given by  $F[\phi_A, w_A, \phi_B, w_B, \xi]$ , where  $\phi_A$ ,  $w_A$ ,  $\phi_B$ ,  $w_B$ , and  $\xi$  are the functions for which  $F$  attains its minimum. From the definition of  $F$ , Eq. (7), it follows that these functions satisfy the self-consistent equations,

$$w_A(\mathbf{r}) = \chi N \phi_B(\mathbf{r}) - H(\mathbf{r}) N + \xi(\mathbf{r}), \quad (9)$$

$$w_B(\mathbf{r}) = \chi N \phi_A(\mathbf{r}) + H(\mathbf{r}) N + \xi(\mathbf{r}), \quad (10)$$

$$\phi_A(\mathbf{r}) + \phi_B(\mathbf{r}) = \Phi_0(\mathbf{r}), \quad (11)$$

$$\phi_A = - \frac{\mathcal{V}}{\mathcal{Q}} \frac{\mathcal{D}\mathcal{Q}}{\mathcal{D}w_A}, \quad (12)$$

$$\phi_B = - \frac{\mathcal{V}}{\mathcal{Q}} \frac{\mathcal{D}\mathcal{Q}}{\mathcal{D}w_B}. \quad (13)$$

The last two equations identify  $\phi_A(\mathbf{r})$  and  $\phi_B(\mathbf{r})$  as the average densities of A and B segments at  $\mathbf{r}$  as calculated in the ensemble of the non-interacting polymers subject to external fields,  $w_A(\mathbf{r})$  and  $w_B(\mathbf{r})$ . The fields are calculated self-consistently from Eqs. (9), (10), and (11). The details on how to solve Eqs. (9)–(13) to obtain the SCFT free energy are provided in the Appendix.

Previous work<sup>19,20</sup> on block copolymer films has employed the strong-segregation theory (SST) of Semenov.<sup>14</sup> So that we can compare their results with our more accurate calculation, we recast the equations of the SST in terms of our present definitions. The free energy  $F$  of a lamellar structure is given by

$$\begin{aligned}
\frac{F}{nk_B T} = \frac{\pi^2}{32} \left( \frac{D}{aN^{1/2}} \right)^2 + 2 \left( \frac{\chi N}{6} \right)^{1/2} \left( \frac{D}{aN^{1/2}} \right)^{-1} \\
+ \left( (1 - 2\psi_1) \Lambda_1 N + (1 - 2\psi_2) \Lambda_2 N \right. \\
\left. + \frac{\pi^2}{24} \left( \frac{\epsilon}{aN^{1/2}} \right)^{-1} \right) \left( \frac{\Delta}{aN^{1/2}} \right)^{-1}, \quad (14)
\end{aligned}$$

where  $\psi_1$  is the fraction of the  $x=0$  surface covered by component A and  $\psi_2$  is the coverage of the  $x=\Delta_0$  surface. The term involving  $\epsilon$  is the loss of conformation entropy at the two surfaces and is given by<sup>14,21</sup>

$$\frac{F_{\text{conf}}}{nk_B T} = \frac{a^2 N}{24 \mathcal{V}} \int d\mathbf{r} |\nabla \Phi_0(\mathbf{r})|^2 \Phi_0^{-1}(\mathbf{r}). \quad (15)$$

In a parallel lamellar ( $L_v^\parallel$ ) phase,  $\psi_1$  and  $\psi_2$  take on values of 0 or 1, and  $D=2\Delta/\nu$ . For the perpendicular lamellar ( $L^\perp$ ) phase,  $\psi_1=\psi_2=0.5$ , and the domain spacing relaxes to the bulk spacing,

$$\frac{D_b}{aN^{1/2}} = 2 \left( \frac{8}{3\pi^4} \right)^{1/6} (\chi N)^{1/6}. \quad (16)$$

We note that in the  $L^\perp$  phase, the lamellae are assumed to be perfectly flat. In reality, variations in their width will occur near the surfaces causing small deviations from  $\psi_1=\psi_2=0.5$  towards more energetically favorable values. While this is difficult to account for in the SST, the SCFT described above does so automatically. We do not examine the  $L_v^M$  phases using SST, because any reasonable treatment would be difficult.

### III. RESULTS

Unless otherwise stated, the results presented below are for symmetric diblocks ( $f=0.5$ ) at an intermediate degree of segregation ( $\chi N=20$ ) between walls possessing identical surface potentials ( $\Lambda \equiv \Lambda_1 = \Lambda_2$ ). Furthermore, the distance from the walls over which the segment density rises to the bulk value is taken to be  $\epsilon/aN^{1/2}=0.15$ . This width is small enough relative to the domains such that its finite size does not significantly influence phase behavior. Reducing  $\epsilon/aN^{1/2}$  further does little other than increase the number of basis functions required to perform accurate calculations (see the Appendix). Under the conditions examined here, we found 225 functions to be sufficient, which is a number that can be handled on a moderate size computer.

We begin in Fig. 2 with plots analogous to one in Ref. 19 showing the minimum free energy among the  $L_v^\parallel$  phases (solid curves) compared to that of the  $L^\perp$  phase (dashed curves) as a function of film thickness  $\Delta$  with a fixed surface field ( $\Lambda N=0.2$ ). Results are calculated using both SCFT and SST. Rather than simply showing the free energy, we plot  $(F - F_b)\Delta/nk_B T a N^{1/2}$ , where  $F_b$  is the bulk free energy. This quantity is proportional to the excess free energy per unit area (i.e., the surface tension of the film), and is important when considering unconfined films. On the horizontal axis, the film thickness is normalized with respect to the bulk domain spacing  $D_b$ . In this way, differences between the

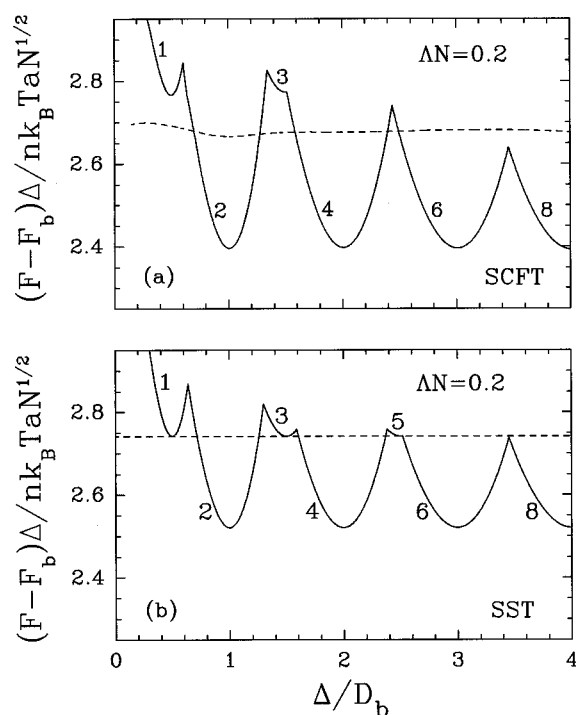


FIG. 2. Free energy  $F$  as a function of film thickness  $\Delta$  for the  $L_\nu$  phases (solid curves) and the  $L^\perp$  phase (dashed curves) calculated using (a) SCFT and (b) SST. The calculations are performed with  $\epsilon/aN^{1/2}=0.15$ ,  $\chi N=20$ ,  $f=0.5$ , and  $\Lambda_1 N = \Lambda_2 N = \Lambda N = 0.2$ . To mask some of the inaccuracies of the SST, results are normalized with respect to the bulk free energy  $F_b$  and the bulk lamellar period  $D_b$ . In SCFT,  $F_b/nk_B T = 3.985$  and  $D_b/aN^{1/2} = 1.651$ , where as in SST,  $F_b/nk_B T = 3.029$  and  $D_b/aN^{1/2} = 1.809$ .

SCFT and SST plots due to inaccuracies in the SST predictions of  $F_b$  and  $D_b$  are masked, enhancing the more minor differences. In particular, this reveals a small vertical shift between the solid and dashed curves, which breaks the degeneracy between the  $L_\nu$  and  $L^\perp$  phases predicted by SST at half integer values of  $\Delta/D_b$ .

One clear advantage of the present SCFT approach over the SST one is the ease with which complicated microstructures (e.g.,  $L_\nu^M$ ) can be treated. Here microstructures are examined under conditions where the mixed lamellar ( $L_\nu^M$ ) phases are most favored, i.e., film thicknesses where the symmetric lamellar ( $L_\nu$ ,  $\nu=2,4,6,\dots$ ) phases are most frustrated. Figure 3 shows the domains of various phases with  $\Lambda N=0.2$  and  $\Delta$  chosen so that  $L_2^\parallel$  and  $L_4^\parallel$  are equal in free energy. At the top, the A segment profiles,  $\phi_A(\mathbf{r})$ , of the  $L_\nu^\parallel$  phases are plotted. The domains of the  $L_2^\parallel$  phase are highly stretched and those of the  $L_4^\parallel$  phase are highly compressed relative to the bulk spacing  $D_b$ . Although the  $L_3^\parallel$  phase has a period close to  $D_b$ , there is an unfavorable B domain next to the right wall. In each of the  $L_\nu^\parallel$  phases, all the interior domains are nearly identical in width as are all the interfaces between them,<sup>22</sup> consistent with experimental observation.<sup>9</sup> The interfacial width  $w$  does vary among the phases; for the  $L_2^\parallel$ ,  $L_3^\parallel$ , and  $L_4^\parallel$  phases in Fig. 3,  $w/aN^{1/2} = 0.318, 0.275$ , and  $0.262$ , respectively, as compared to  $0.280$

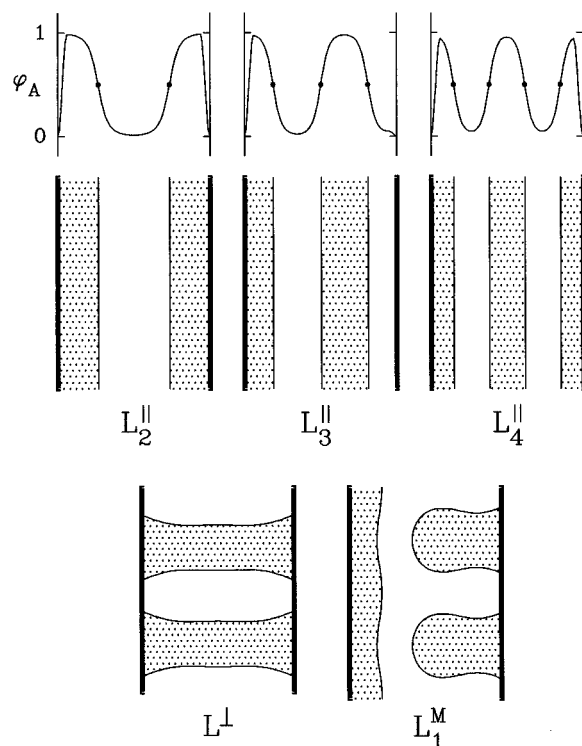


FIG. 3. Domain shapes in the  $L_2^\parallel$ ,  $L_3^\parallel$ ,  $L_4^\parallel$ ,  $L^\perp$ , and  $L_1^M$  phases calculated for a film of thickness  $\Delta/aN^{1/2} = 2.296$  between walls each with a surface potential  $\Lambda N = 0.2$ . Under this condition,  $L_2^\parallel$  and  $L_4^\parallel$  are equal in free energy. Bold lines denote the hard walls and textured regions represent the A domains. For the  $L_\nu^\parallel$  phases, the A segment distribution across the film is shown above with dots indicating the A/B interfaces at  $\phi_A(\mathbf{r}) = \phi_B(\mathbf{r})$ .

in the bulk. Again, this is consistent with experiment.<sup>1</sup>

Figure 4 shows the free energy of the  $L_2^\parallel$ ,  $L_3^\parallel$ ,  $L_4^\parallel$ ,  $L^\perp$ , and  $L_1^M$  phases as a function of surface potential along the path where  $L_2^\parallel$  and  $L_4^\parallel$  are equal in free energy. Under this condition,  $L^\perp$  is the stable phase. We have searched for a  $L_0^M$  phase, but our unsuccessful attempts suggest that this phase is not even metastable. From Eq. (14) it follows that the curves in Fig. 4 have slopes of  $2(1-\psi_1-\psi_2) \times (\Delta/aN^{1/2})^{-1}$ , where  $\psi_1$  is the fraction of surface 1 covered

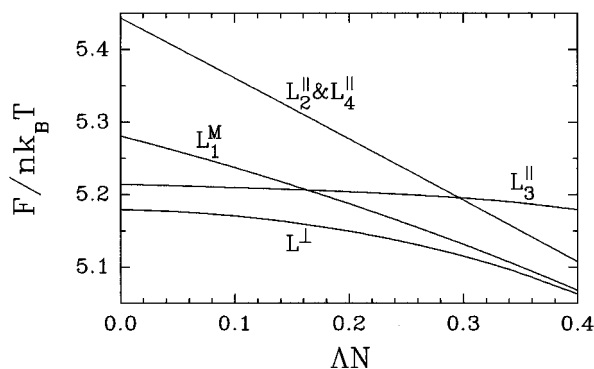


FIG. 4. Free energies  $F$  of the phases shown in Fig. 3 as a function of surface potential  $\Delta N$  with the film thickness  $\Delta$  varied to maintain  $L_2^\parallel$  and  $L_4^\parallel$  at the same free energy, so that they are equally frustrated.

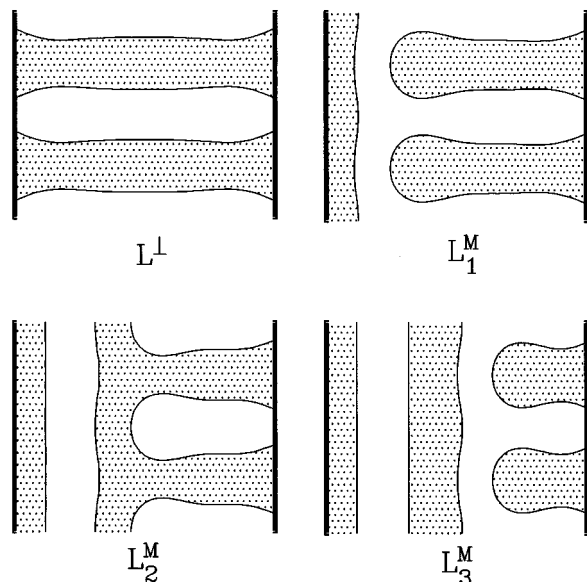


FIG. 5. Similar to Fig. 3 except that phases are examined at  $\Delta N=0.2$  and  $\Delta/aN^{1/2}=4.027$ , where  $L_4^||$  and  $L_6^||$  are equal in free energy. The less interesting parallel lamellar phases have been omitted. The domains are shown on the same scale as those in Fig. 3.

by component A and  $\psi_2$  is the same for surface 2. (Although Eq. (14) is a SST expression, this result still holds for SCFT with the appropriate definitions of  $\psi_1$  and  $\psi_2$ .) At  $\Delta N=0.0$ ,  $\psi_1=\psi_2=0.5$  in the  $L^\perp$  phase, and therefore the slope of its free energy is zero. On the other hand,  $\psi_1 \approx 1.0$  and  $\psi_2 \approx 0.5$  in the  $L_1^M$  phase, producing a negative slope. Thus as  $\Delta N$  increases from zero,  $L_1^M$  becomes less unstable relative to  $L^\perp$ . However, a positive  $\Delta N$  attracts A segments to the surface (see Fig. 3) causing the slopes to change. By  $\Delta N=0.4$ , the potential is so strong that  $\phi_1 \approx \phi_2 \approx 1.0$  in both the  $L^\perp$  and  $L_1^M$  phases, and beyond this point increasing  $\Delta N$  has little effect on their relative stability.

Moving to thicker films, we examine the stability of phases along the path where  $L_4^||$  and  $L_6^||$  are equal in free energy. Figure 5 shows the domain shapes of the  $L^\perp$  and  $L_\nu^M$  phases at a surface potential of  $\Delta N=0.2$ ; the  $L_\nu^||$  phases are omitted because they are uninteresting. The three  $L_\nu^M$  phases all have very similar regions separating the parallel and perpendicular lamellae. Notably, these regions are narrow; for example, only the innermost parallel A/B interface shows any significant curvature. In the  $L^\perp$ ,  $L_1^M$ ,  $L_2^M$ , and  $L_3^M$  phases, the perpendicular lamellae have periods of  $D/aN^{1/2} = 1.649, 1.676, 1.685$ , and  $1.698$ , respectively, as compared to the bulk period  $D_b/aN^{1/2} = 1.651$ . The periods of the  $L_\nu^M$  phases are all slightly larger than  $D_b$  because of the enlarged caps at the ends of the perpendicular lamellae. We note that these enlarged ends have been observed experimentally at grain boundaries in the lamellar phase.<sup>23</sup>

Figure 6 presents a plot similar to the one in Fig. 4, except now  $\Delta$  is chosen so that  $L_4^||$  and  $L_6^||$  are equal in free energy. In this case, a triple point exists at  $\Delta N=0.250$  below which  $L^\perp$  is stable and above which  $L_4^||$  and  $L_6^||$  are stable. Of the mixed lamellar phases,  $L_1^M$  has the lowest energy just

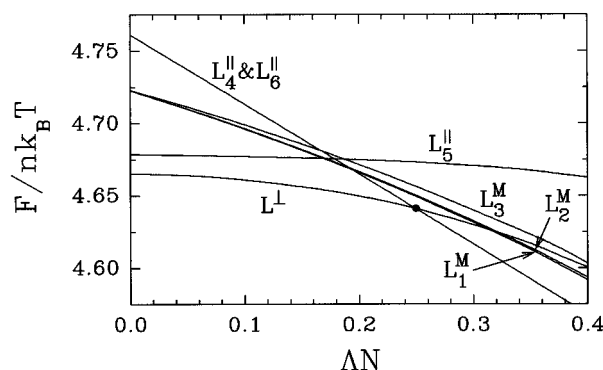


FIG. 6. Similar to Fig. 4 except that here the film thickness is varied to keep the free energies of  $L_4^||$  and  $L_6^||$  equal. The dot denotes a phase transition between perpendicular and parallel lamellae.

slightly less than that of  $L_2^M$ . Nevertheless, even at the triple point where the mixed lamellar phases are favored most, they are far more unstable than the  $L_1^M$  phase was in Fig. 4. This is because thicker films have more lamellae over which to accommodate a mismatch in  $\Delta$  and  $D_b$ . Hence there is less frustration, and thus less advantage to forming a  $L_\nu^M$  phase.

Now that we know the  $L_\nu^M$  phases are unstable, we are ready to construct a phase diagram. Figure 7 shows diagrams for symmetric diblocks at  $\chi N=20$  and equal surface poten-

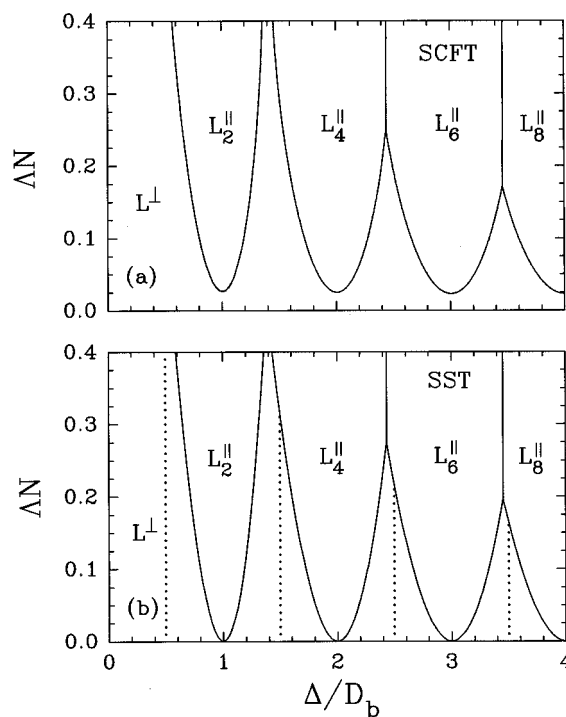


FIG. 7. Phase diagram for intermediately segregated ( $\chi N=20$ ) symmetric diblock ( $f=0.5$ ) films confined between identical walls calculated using (a) SCFT and (b) SST. Each diagram is plotted in terms of the film thickness  $\Delta$  relative to the bulk lamellar period  $D_b$  vs the surface potential  $\Delta N \equiv \Delta_1 N = \Delta_2 N$ . In the SST, the antisymmetric parallel phases become degenerate in free energy with the  $L^\perp$  phase along the dotted lines.

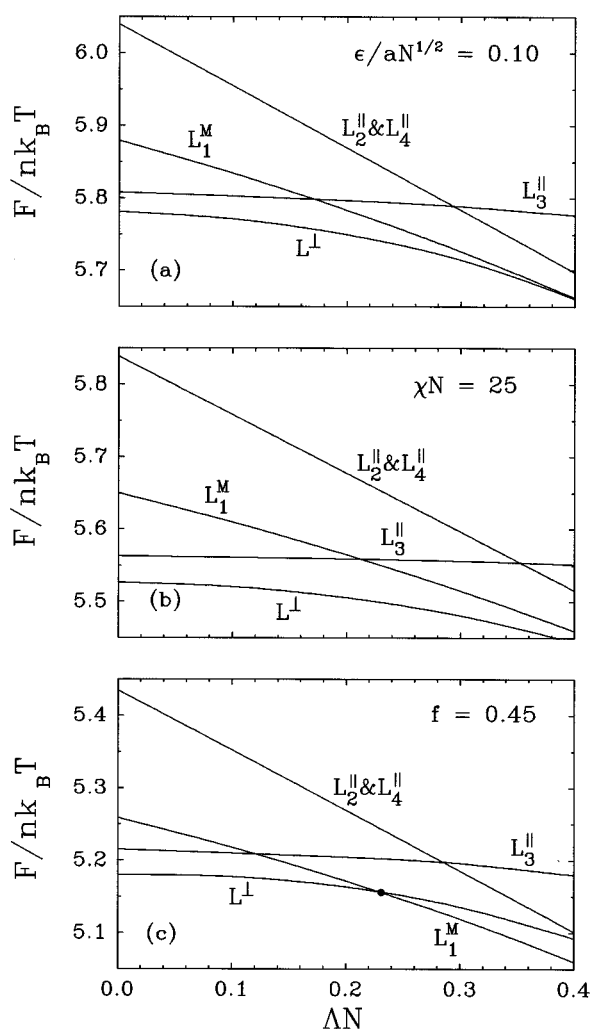


FIG. 8. Free energy plots along the path where  $L_2^||$  and  $L_4^||$  have identical energy. They are analogous to Fig. 4 where  $\epsilon/aN^{1/2}=0.15$ ,  $\chi N=20$ , and  $f=0.50$ , but (a) is for a narrower surface profile  $\epsilon/aN^{1/2}=0.10$ , (b) is for a high degree of segregation  $\chi N=20$ , and (c) is for an asymmetric diblock  $f=0.45$ . In the latter case, the dot denotes a phase transition between the  $L^\perp$  and  $L_1^M$  phases.

tials (i.e.,  $\Lambda \equiv \Lambda_1 = \Lambda_2$ ) calculated using SCFT and SST. The two theories produce very similar phase diagrams, but there are two notable differences between them. First, the antisymmetric  $L_\nu^||$  phases ( $\nu=1,3,4,\dots$ ) do not become degenerate with the  $L^\perp$  phase in the SCFT phase diagram. Second, the  $L_\nu^||$  phases in the SCFT diagram do not extend down to  $\Delta N=0.0$ . We attribute these differences to a negative line tension where the A/B interface intersects the surface (see Sec. IV). Such a line tension, which is not accounted for in the SST, would favor the  $L^\perp$  phase.

Up to this point,  $\epsilon/aN^{1/2}$ ,  $\chi N$ , and  $f$  have been held fixed at 0.15, 20, and 0.5, respectively. In order to assess their effect on phase behavior, we repeat Fig. 4 separately varying each of the parameters. In Fig. 8(a),  $\epsilon/aN^{1/2}$  is decreased to 0.10. This causes a significant increase in the free energy consistent with the larger entropic surface energy predicted by Eq. (15). However, the relative stability of the

phases is largely unaffected (i.e., the curves cross at about the same values of  $\Delta N$  as in Fig. 4). Next, Fig. 8(b) shows the effect of increasing  $\chi N$  to 25. Naturally, increasing the segregation causes a rise in the free energy. Also, the locations where the curves cross have moved to larger  $\Delta N$ . Presumably, they are shifted by a factor approximately equal to the increase in the A/B interfacial tension. Lastly, Fig. 8(c) is calculated with  $f=0.45$ . We chose  $f<0.5$ , because this produces a spontaneous curvature in the A/B interface favoring the domain shapes in the  $L_1^M$  phase (see Fig. 4). Indeed, the  $L_1^M$  phase is now stable for  $\Delta N>0.231$ . No doubt, the same effect could be achieved by introducing conformational asymmetry with the A segment length larger than the B segment length.

Our attention has been restricted to identical surface potentials (i.e.,  $\Lambda \equiv \Lambda_1 = \Lambda_2$ ). For completeness, we now examine the phase behavior of films with  $\Lambda_1 \neq \Lambda_2$ . To do this, we use SST because it is numerically simple and has proved to be reliable (see Fig. 7). The only concern is how to account for possible  $L_\nu^M$  phases, but for the moment we ignore them. Without loss of generality, the surface with the greatest potential is labeled as 1 and the segments that it attracts are labeled A (i.e.,  $\Lambda_1 \geq |\Lambda_2|$ ). By doing this, it is sufficient to examine the evolution of the phase diagram as  $\Lambda_2/\Lambda_1$  varies from 1.0 to  $-1.0$ ; this is done in Fig. 9. At  $\Lambda_2/\Lambda_1=1.0$ , the phase diagram is the same as in Fig. 7(b) where the antisymmetric  $L_\nu^||$  phases ( $\nu=1,3,5,\dots$ ) only occur along one-dimensional lines at half integer values of  $\Delta/D_b$ . As  $\Lambda_2/\Lambda_1$  decreases, these lines open up into two-dimensional regions [see Fig. 9(b)]. Note that for high surface potentials, the antisymmetric phases are squeezed out in favor of the symmetric ones. At  $\Lambda_2/\Lambda_1=0.0$ , all the  $L_\nu^||$  phases have comparable widths and all of them extend to  $\Lambda_1 N=\infty$ . As  $\Lambda_2/\Lambda_1$  becomes negative and decreases to  $-1.0$ , the symmetric  $L_\nu^||$  regions are reduced to one-dimensional lines at integer values of  $\Delta/D_b$  [see Fig. 9(e)]. If the  $L_\nu^M$  phases were to occur in Fig. 9, they would be most stable at the two extremes,  $\Lambda_2/\Lambda_1=\pm 1.0$ , where the domain spacing of the  $L_\nu^||$  phases is most frustrated. In these two limits, SCFT predicts the  $L_\nu^M$  phases to be unstable, and so we conclude that they are unstable for all ratios of  $\Lambda_2/\Lambda_1$ .

The above calculations for confined films can be used to predict the phase behavior of unconfined films. In the unconfined case, where one surface is for example air, a uniform film of thickness  $\Delta$  can separate into two coexisting phases with thicknesses  $\Delta'$  and  $\Delta''$ . Conservation of material requires

$$\Delta = \theta \Delta' + (1 - \theta) \Delta'', \quad (17)$$

where  $\theta$  is the area fraction of the film with thickness  $\Delta'$ . The free energy of the phase separated film is

$$F = [\theta F(\Delta') \Delta' + (1 - \theta) F(\Delta'') \Delta''] / \Delta, \quad (18)$$

where  $F(\Delta)$  refers to the free energy of a uniform film of thickness  $\Delta$ . Minimizing Eq. (18) subject to the constraint in Eq. (17) gives the condition of metastability,

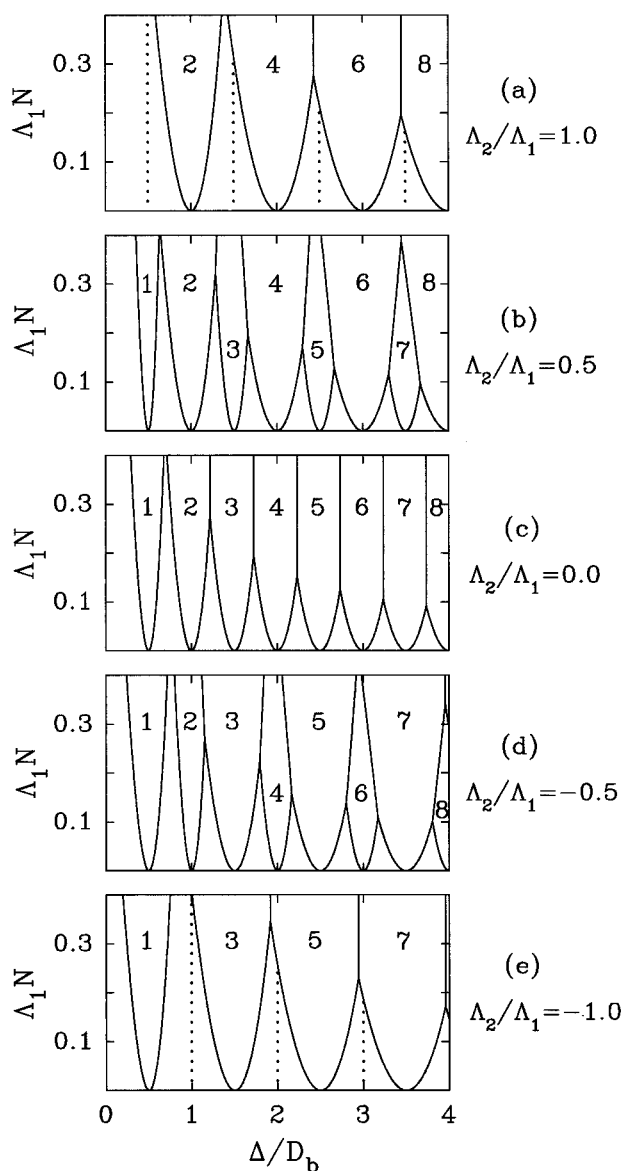


FIG. 9. Phase diagrams calculated using SST for unequal surface potentials. The stronger surface potential is denoted as  $\Lambda_1$ , and then the ratio  $\Lambda_2/\Lambda_1$  is varied from 1.0 to  $-1.0$ . The  $L_\nu^\parallel$  regions are labeled by their index  $\nu$ , and the  $L^\perp$  regions are unlabeled.

$$\begin{aligned} \frac{d}{d\Delta} F(\Delta)\Delta|_{\Delta=\Delta'} &= \frac{d}{d\Delta} F(\Delta)\Delta|_{\Delta=\Delta''} \\ &= \frac{F(\Delta')\Delta' - F(\Delta'')\Delta''}{\Delta' - \Delta''}. \end{aligned} \quad (19)$$

The solution to these equations can be obtained using the double-tangent construction illustrated in Fig. 10. Once  $\Delta'$  and  $\Delta''$  are known,  $\theta$  can be determined by the lever rule,

$$\theta = \frac{\Delta - \Delta''}{\Delta' - \Delta''}, \quad (20)$$

which follows directly from Eq. (17). The free energy of the phase separated film is given by the value of the double-tangent line at  $\Delta$ . In Fig. 10, we consider a film prepared

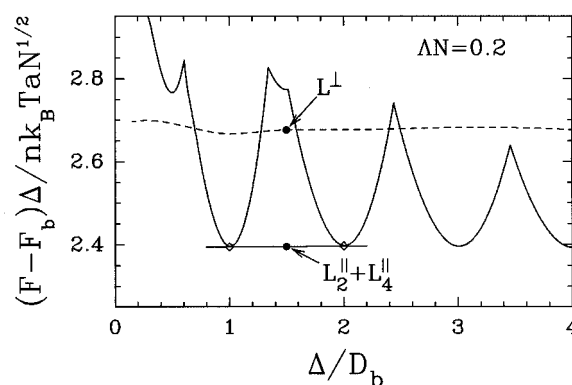


FIG. 10. Illustration of the double-tangent construction for unconfined films using the plot shown earlier in Fig. 2(a). Here, we consider a film with an average thickness  $\Delta/D_b = 1.5$ . If this film was constrained to a uniform thickness, then it would exist in the  $L^\perp$  phase with a free energy denoted by the upper dot. Without confinement, the film phase separates into  $L_2^\parallel + L_4^\parallel$  lowering its energy to the value denoted by the dot on the double-tangent line. The diamonds denote the two thicknesses of the phase-separated film.

with a uniform thickness  $\Delta = 1.5D_b$  in the  $L^\perp$  phase, where it has a free energy of  $F/nk_B T = 2.676$ . By separating into the  $L_2^\parallel$  and  $L_4^\parallel$  phases with thicknesses  $\Delta' \approx D_b$  and  $\Delta'' \approx 2D_b$ , respectively, the free energy is lowered to  $F/nk_B T = 2.395$ . Experiments<sup>4</sup> indicate that under appropriate conditions a narrow region of  $L^\perp$  remains at the interface between the  $L_2^\parallel$  and  $L_4^\parallel$  phases. Note that phase separating into  $L_2^\parallel + L_6^\parallel$  also lowers the free energy; according to SST it causes the exact same reduction in energy, and with SCFT we find it to be the same to within our numerical resolution. Nevertheless, if the system starts off with a uniform thickness, it will first encounter the  $L_2^\parallel + L_4^\parallel$  state and then presumably be kinetically trapped there. With this in mind, Fig. 11 shows a schematic phase diagram for unconfined films initially prepared with a uniform thickness, where both surfaces have the same preferential affinity for component A. The unconfined struc-

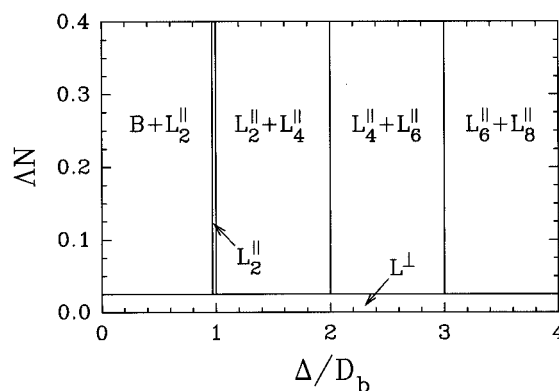


FIG. 11. Schematic phase diagram for unconfined films under equivalent conditions to those for the confined films in Fig. 7(a). Here, we assume that the tension of a bare (B) substrate is sufficiently large that the film does not dewet. Although the  $L_2^\parallel$  one-phase region can be resolved on the scale of this plot, those of the other parallel lamellar phases cannot. Likewise, the  $L^\perp + L_\nu^\parallel$  coexistence regions are too narrow to resolve.



tures all adopt domain spacings very close to the bulk spacing in agreement with experiment,<sup>5</sup> contrary to concerns raised in Ref. 24. To produce the phase diagram for unconfined films, the surface tension of the air/substrate interface is required. That is we must know where the curve in Fig. 10 terminates at  $\Delta/D_b=0.0$ , so that the boundary between the  $B+L_2$  and  $L_2$  regions can be evaluated ( $B$  represents the bare substrate). Naturally, this tension depends on the interactions between the air and the substrate, which are not considered in our model. So to construct Fig. 11, we have arbitrarily assumed a value of  $\sim 2.7$ . Note that if we chose a value less than  $\sim 2.4$ , the block copolymer film would dewet from the substrate.

#### IV. DISCUSSION

There are a number of advantages of our present approach over previous ones. Although strong-segregation calculations are attractive because they are easy to implement and produce nice analytical results, they do suffer from a number of limitations. For example, the SST requires *a priori* assumptions regarding the shape of the A/B interface, and for nontrivial shapes calculations become difficult. This is why our SST calculation for the  $L^\perp$  phase<sup>19</sup> assumes flat interfaces, and why no attempt was made to consider the  $L_v^M$  phases within SST. Furthermore, the SST assumes the polymer chains are strongly stretched, which is generally not the case; this can result in unreliable predictions.<sup>25</sup> Weak-segregation calculations<sup>26,27</sup> have the virtue that fluctuation corrections are possible,<sup>26</sup> but still they present their own limitations; the most significant being that they are unable to treat intermediate degrees of segregation typical of experiments. Other studies<sup>28</sup> use a phenomenological model with parameters that are not clearly related to the molecular parameters (i.e.,  $\chi$ ,  $N$ , and  $f$ ), limiting the interpretation of their results. Furthermore, this approach treats chain stretching in an artificial way that may misrepresent the effects of packing frustration. Monte Carlo simulations<sup>11,29</sup> have the advantage that no assumptions about the microstructure are required, but they are numerically intensive and can suffer from finite-size limitations<sup>30</sup> as well as nonequilibrium effects discussed below. Pickett and Balazs<sup>31</sup> have applied the SCFT of Scheutjens and Fleer<sup>32</sup> to describe thin films. This approach is very similar to ours except that it restricts configurations of the polymers to some arbitrary, unphysical lattice. The present SCFT approach of Helfand<sup>12</sup> avoids many of the above limitations and is based on a well established microscopic model that can be generalized to consider more complex systems. For example, a more realistic treatment of the surfaces is possible using an equation-of-state treatment for the compressibility.<sup>17</sup> The flexible Gaussian polymers can be replaced with semi-flexible worm-like ones.<sup>33</sup> Other block copolymer architectures can be easily treated.<sup>34</sup> Furthermore, there is no difficulty in considering multicomponent systems, e.g., including a solvent or a homopolymer species.<sup>35</sup> The most serious limitation of the SCFT is that *a priori* knowl-

edge of the possible microstructures is required, but this can be provided by experiment and Monte Carlo results as was the case for the  $L_v^M$  phases.

The results presented above have assumed both the shape and the width  $\epsilon$  of the segment profile at the surfaces. For hard walls (e.g., silicon), a more accurate treatment would determine the surface profile and its width through a competition between compressibility of the melt which favors small  $\epsilon$  and entropic surface energy [i.e., Eq. (15)] which favors large  $\epsilon$ . On the other hand, soft walls composed of an immiscible polymer (i.e., a random AB copolymer<sup>8</sup>) should be treated differently. In this case, the width of the surface profile is set by a competition between unfavorable segment interactions and the entropic surface energy in the same way that the internal A/B interfacial width is determined.<sup>14</sup> The variety of possible surfaces would produce a large range of widths, of which  $\epsilon/aN^{1/2}=0.15$  could be considered an intermediate value. One hopes that the behavior of the film depends weakly on the details of the surface, and our calculations support this. Nevertheless, surface details are not completely irrelevant. Here, we find that the surface energy varies between parallel and perpendicular orientations of the lamellae, and in particular, it favors the perpendicular orientation. The lattice SCFT calculation by Pickett and Balasz<sup>31</sup> also finds this. On the other hand, this effect is not captured by our SST calculation. Pickett *et al.*<sup>36</sup> have proposed several mechanisms that could distinguish between parallel and perpendicular orientations, but none would explain our SCFT results for Gaussian chains. Instead, we suggest that there is a negative line tension at intersections between the A/B interfaces and the surfaces. This could occur if the presence of an intersection caused a local decrease in either the surface tension or the A/B interfacial tension. In principle, a more detail SST treatment of these intersections could evaluate the line tension, but that is beyond the scope of this paper.

The fact that SST produces a phase diagram similar to our SCFT one implies that phase behavior changes very little for  $\chi N \geq 20$ . This is further supported by our calculation at  $\chi N = 25$  in Fig. 6(b). More specifically, if the phase diagram is plotted in terms of the scaled quantities  $\Delta N/(\chi N)^{1/2}$  and  $\Delta/D_b$ , then it should only exhibit a weak dependence on  $\chi N$ . Naturally, this will not remain true as the weak-segregation regime is approached, i.e.,  $\chi N \sim 11$ . In this regime, surface potentials can produce interesting effects on the order-disorder transition.<sup>6,13,26,29</sup> We have not examined weakly segregated films, partly because this is where the mean-field approximation breaks down.<sup>26</sup> We note that even though the SST phase diagram approximates our SCFT one well at  $\chi N = 20$ , the details of the individual phases such as their free energies, segment distributions, and domain spacings are poorly approximated.

In confined films, phase behavior appears to be much more sensitive to the "spontaneous" curvature of the interface than in the bulk. The symmetric molecules (i.e.,  $f=0.5$ ) examined here favor flat interfaces. As a result, the bulk forms a lamellar phase, and the thin films form  $L_v$  and  $L^\perp$  phases. In the bulk, the lamellar phase persists up to

rather high asymmetries ( $f \sim 0.34$ ) before a transition occurs to a curved structure (i.e., the gyroid phase).<sup>2</sup> On the other hand, just a small asymmetry is sufficient to produce a phase transition in the film and stabilize, for example, the  $L_1^M$  phase [see Fig. 6(c)]. Accordingly, we can expect a far richer phase behavior in thin films than observed in the bulk. Furthermore, the addition of homopolymer or solvent should have particularly dramatic effects due to the high degrees of packing frustration that occur in confined films.

Caution should be taken in interpreting experimental or even Monte Carlo results as equilibrium phase behavior. Polymer systems can be very slow to equilibrate and can exist in metastable states for prolonged times. In bulk samples, this has led researchers to conclude the existence of a stable perforated lamellar phase when in fact the gyroid phase was more stable.<sup>37</sup> Efforts to understand the importance of kinetic pathways in bulk phase behavior are presently underway.<sup>38</sup> Similar care needs to be taken in the study of thin films. The  $L_v^M$  phases observed in experiment<sup>9</sup> and Monte Carlo simulations<sup>11</sup> may actually be unstable compared to the  $L^\perp$  phase, consistent with our prediction. The  $L_v^M$  phases may occur simply because their kinetic pathways are more accessible. When a disordered film is quenched into the order state, presumably the surface fields cause lamellae to nucleate at the surfaces with a parallel orientation and the bulk domain spacing. Only when these regions grow large enough that they encounter the opposite surface will the mismatch between the domain spacing  $D_b$  and the film thickness  $\Delta$  become evident. At this point, the easiest solution to the problem is to form a  $L_v^M$  phase. Because surface fields disfavor perpendicular lamellae, the  $L^\perp$  phase is suppressed. If perpendicular grains do become large enough to span the film, they should continue to grow at the expense of the  $L_v^M$  phase. However, this growth may be exceptionally slow since the energy difference between the two phases can be very small.

## V. SUMMARY

We have developed a method for examining arbitrary periodically ordered microstructures in block copolymer thin films using self-consistent field theory. Here the method is applied to symmetric AB diblock copolymers confined between two identical parallel walls. Generally, surface fields favor lamellar structures that are aligned parallel with the walls. However, in a confined film where the thickness is highly incommensurate with the bulk period, the lamellae may orient perpendicular to the walls. Experiments and Monte Carlo simulations have suggested that a mixed lamellar phase may also occur when parallel lamellae are sufficiently frustrated. However, our calculation predicts such phases to be slightly unstable relative to perpendicular lamellae. This raises the possibility that the mixed lamellar phases are observed because they are kinetically favored rather than because they are equilibrium structures. Notably, we do predict a stable mixed lamellar phase when a small spontaneous curvature in the A/B interface is produced by an asymmetry in the molecule (e.g.,  $f \neq 0.5$ ). When confinement is re-

moved, films generally phase separate into coexisting parallel lamellar phases each with approximately the bulk domain spacing. If the surface fields are small then a parallel lamellar phase can occur in an unconfined film, presumably because of a negative line tension where A/B interfaces intersect the surfaces.

Confined films offer a unique opportunity to examine frustration in block copolymer microstructures. Because of this frustration, we anticipate a much richer phase behavior than that produced by bulk melts. We have already demonstrated an enhanced sensitivity to the molecular composition  $f$ , and no doubt conformational asymmetry will have a similar impact on phase selection. Cylinder- and sphere-forming block copolymers are likely to exhibit even more interesting behavior,<sup>27,39</sup> particularly when the minority domain is attracted to the surfaces. Furthermore, interesting phenomena can be anticipated with the addition of homopolymer or solvent because of the elevated degrees of frustration. Likewise, block copolymer blends are bound to produce interesting results particularly if the individual constituents favor different domain sizes. Experimental studies have already illustrated that films are ideal for the study of electric fields on microdomain formation.<sup>3</sup> The study of block copolymer films has just begun, and we expect continued efforts to generate a wealth of interesting phenomena.

## ACKNOWLEDGMENTS

We are grateful to N. Koneripalli, F. S. Bates, and G. T. Pickett for useful discussions, and to the Department of Chemical Engineering and Materials Science at the University of Minnesota where this work was initiated.

## APPENDIX

Here we provide the details for solving the self-consistent field equations (9)–(13) in Sec. II. The first step is to evaluate the partition function  $\mathcal{Q}[w_A, w_B]$ . To do this, we express it as an integral,

$$\mathcal{Q} = \int d\mathbf{r} q(\mathbf{r}, 1), \quad (\text{A1})$$

where

$$\begin{aligned} q(\mathbf{r}, s) = & \int \mathcal{D}\mathbf{r}_\alpha P[\mathbf{r}_\alpha; 0, s] \delta(\mathbf{r} - \mathbf{r}_\alpha(s)) \\ & \times \exp \left\{ - \int_0^s dt [\gamma(t) w_A(\mathbf{r}_\alpha(t)) \right. \\ & \left. + (1 - \gamma(t)) w_B(\mathbf{r}_\alpha(t))] \right\} \end{aligned} \quad (\text{A2})$$

is an end-segment distribution function. The function  $\gamma(s)$  is defined to be 1 when  $s$  corresponds to an A-segment region of the copolymer and is 0 for a B-segment region. This distribution function satisfies the modified diffusion equation,

$$\frac{\partial}{\partial s} q(\mathbf{r}, s) = \begin{cases} \frac{1}{6} Na^2 \nabla^2 q(\mathbf{r}, s) - w_A(\mathbf{r}) q(\mathbf{r}, s), & \text{if } 0 < s < f, \\ \frac{1}{6} Na^2 \nabla^2 q(\mathbf{r}, s) - w_B(\mathbf{r}) q(\mathbf{r}, s), & \text{if } f < s < 1, \end{cases} \quad (\text{A3})$$

with  $q(\mathbf{r}, s) = 0$  at each surface and  $q(\mathbf{r}, 0) = 1$  for all points inside the film.<sup>12</sup> Because the two ends of the molecule are distinct, a second end-segment distribution function,  $q^\dagger(\mathbf{r}, s)$  is defined with an almost identical definition, Eq. (A2), except that the functional integral over  $\mathbf{r}_\alpha(t)$  is done for  $t = s$  to 1. In this case,  $q^\dagger(\mathbf{r}, s) = 0$  at each surface,  $q^\dagger(\mathbf{r}, 1) = 1$  for all points inside the film, and it satisfies Eq. (A3) with the right-hand side multiplied by  $-1$ . In terms of these functions, the A-segment distribution, Eq. (12), can be written as

$$\phi_A(\mathbf{r}) = \frac{\mathcal{V}}{\mathcal{Q}} \int_0^f ds q(\mathbf{r}, s) q^\dagger(\mathbf{r}, s). \quad (\text{A4})$$

The expression for  $\phi_B(\mathbf{r})$  is similar.

Rather than attempting to solve the above equations in real space, we perform a Fourier series expansion in terms of the basis functions,<sup>18</sup>

$$f_i(\mathbf{r}) = \begin{cases} 2^{1/2} \sin(\pi m_i x / \Delta_0), & \text{if } n_i = 0, \\ 2 \sin(\pi m_i x / \Delta_0) \cos(2\pi n_i y / D), & \text{if } n_i > 0, \end{cases} \quad (\text{A5})$$

where the label  $i = 1, 2, 3, \dots$ ,  $m_i \in \{1, 2, 3, \dots\}$ , and  $n_i \in \{0, 1, 2, \dots\}$ . We order these functions based on the magnitude of their wavevectors. Because they form an infinite series, the set of functions must be truncated in order to perform a calculation. Generally, we start with a small number of functions, and increase the number until our results converge within the resolution of our plots. Our choice of basis functions allows for a microstructure that is periodic in the  $y$ -direction with a period  $D$ , but requires it to be uniform in the  $z$ -direction, which is sufficient for the phases considered here. The extension to phases that are periodic in both the  $y$ - and  $z$ -directions is straightforward. Note that the functions satisfy the orthonormal condition,

$$\frac{1}{\mathcal{V}_0} \int f_i(\mathbf{r}) f_j(\mathbf{r}) d\mathbf{r} = \delta_{ij}, \quad (\text{A6})$$

and are eigenfunctions of the Laplacian operator,

$$\nabla^2 f_i(\mathbf{r}) = -\pi^2 \left( \frac{m_i^2}{\Delta_0^2} + \frac{4n_i^2}{D^2} \right) f_i(\mathbf{r}). \quad (\text{A7})$$

In Fourier space, the diffusion Eq. (A3) becomes

$$\frac{dq_i(s)}{ds} = \begin{cases} \sum_j A_{ij} q_j(s), & \text{if } 0 < s < f, \\ \sum_j B_{ij} q_j(s), & \text{if } f < s < 1, \end{cases} \quad (\text{A8})$$

where the matrix,  $A$ , is given by

$$A_{ij} = -\frac{Na^2 \pi^2}{6} \left( \frac{m_i^2}{\Delta_0^2} + \frac{4n_i^2}{D^2} \right) \delta_{ij} - \sum_k w_{A,k} \Gamma_{ijk}, \quad (\text{A9})$$

with

$$\Gamma_{ijk} = \frac{1}{\mathcal{V}_0} \int f_i(\mathbf{r}) f_j(\mathbf{r}) f_k(\mathbf{r}) d\mathbf{r}. \quad (\text{A10})$$

The matrix,  $B$ , is given by a similar expression. The initial condition becomes  $q_i(0) = I_i$ , where  $I_i$  is the basis function representation of 1. In our present basis,

$$I_i = \frac{2^{1/2}}{\pi m_i} (1 - (-1)^{m_i}) \delta_{n_i, 0}. \quad (\text{A11})$$

This set of linear differential equations can be solved by performing an orthogonal transformation to diagonalize  $A$  if  $s < f$ , or  $B$  if  $s > f$ . The resulting solutions are

$$q_i(s) = \begin{cases} \sum_j T_{A,ij}(s) I_j, & \text{if } 0 \leq s \leq f, \\ \sum_{jk} T_{B,ij}(s-f) T_{A,jk}(f) I_k, & \text{if } f \leq s \leq 1, \end{cases} \quad (\text{A12})$$

$$q_i^\dagger(s) = \begin{cases} \sum_{jk} T_{A,ij}(f-s) T_{B,jk}(1-f) I_k, & \text{if } 0 \leq s \leq f, \\ \sum_j T_{B,ij}(1-s) I_j, & \text{if } f \leq s \leq 1, \end{cases} \quad (\text{A13})$$

where  $T_A(s') \equiv \exp(As')$  and  $T_B(s') \equiv \exp(Bs')$  are matrices that transfer  $q_i(s)$  a distance  $s'$  along the A and B blocks of the molecule, respectively. Similarly, they transfer  $q_i^\dagger(s)$  a distance  $-s'$ .

Once the amplitudes of the end-segment distribution functions are calculated,  $\mathcal{Q}$  is given by  $\mathcal{V}_0 \sum_i q_i(1) I_i$  and the amplitudes of  $\phi_A(\mathbf{r})$ , Eq. (A4), are

$$\phi_{A,i} = \frac{\mathcal{V}}{\mathcal{V}_0 \sum_i q_i(1) I_i} \int_0^f ds \sum_{jk} q_j(s) q_k^\dagger(s) \Gamma_{ijk}. \quad (\text{A14})$$

The amplitudes of  $\phi_B(\mathbf{r})$  are given by a similar expression. Next the amplitudes of the fields,  $w_{A,i}$  and  $w_{B,i}$ , are adjusted so that they satisfy Eqs. (9) and (10),

$$w_{A,i} - w_{B,i} = -\chi N (\phi_{A,i} - \phi_{B,i}) - 2H_i N, \quad (\text{A15})$$

and so that the segment densities satisfy Eq. (11),

$$\phi_{A,i} + \phi_{B,i} = \Phi_{0,i}. \quad (\text{A16})$$

The latter set of conditions are not completely independent, and therefore we replace one of them by the condition,

$$\sum_i \xi_i \Phi_{0,i} = 0. \quad (\text{A17})$$

This completes the cycle of self-consistent equations. To solve them, we need the Fourier amplitudes of  $\Phi_0(\mathbf{r})$ ,

$$\Phi_{0,i} = \frac{2^{-1/2}(1 + \cos(\pi m_i \epsilon / \Delta_0))}{\pi m_i (1 - (m_i \epsilon / \Delta_0)^2)} (1 - (-1)^{m_i}) \delta_{n_i,0}, \quad (\text{A18})$$

and of  $H(\mathbf{r})$ ,

$$H_i = \frac{2^{5/2}(1 - 2(m_i \epsilon / \Delta_0)^2 - \cos(\pi m_i \epsilon / \Delta_0)) a N^{1/2}}{\pi m_i \epsilon (1 - (m_i \epsilon / \Delta_0)^2)} \times (\Lambda_1 - (-1)^{m_i} \Lambda_2) \delta_{n_i,0}. \quad (\text{A19})$$

Once the self-consistent field equations are solved, the free energy, Eq. (7), corresponding to that solution can be written as

$$\frac{F}{n k_B T} = -\ln \left( \sum_i q_i(1) I_i \right) - \chi N \frac{\mathcal{Z}_0}{\mathcal{Z}} \sum_i \phi_{A,i} \phi_{B,i}. \quad (\text{A20})$$

For phases that are periodic in the  $y$ -direction, the free energy must be minimized with respect to  $D$ .

<sup>1</sup>T. P. Russell, *Current Opinion Colloid Interface Sci.* **1**, 107 (1996).

<sup>2</sup>M. W. Matsen and F. S. Bates, *Macromolecules* **29**, 7641 (1996); *J. Chem. Phys.* **106**, 2436 (1997).

<sup>3</sup>T. L. Morkved *et al.*, *Science* **273**, 931 (1996).

<sup>4</sup>B. L. Carvalho and E. L. Thomas, *Phys. Rev. Lett.* **73**, 3321 (1994).

<sup>5</sup>S. H. Anastasiadis, T. P. Russell, S. K. Satija, and C. F. Majkrzak, *J. Chem. Phys.* **92**, 5677 (1990); M. Sikka *et al.*, *Phys. Rev. Lett.* **70**, 307 (1993); *J. Phys. II (France)* **4**, 2231 (1994).

<sup>6</sup>M. D. Foster *et al.*, *J. Chem. Phys.* **96**, 8605 (1992).

<sup>7</sup>S. H. Anastasiadis, T. P. Russell, S. K. Satija, and C. F. Majkrzak, *Phys. Rev. Lett.* **62**, 1852 (1989); G. Coulon, T. P. Russell, V. R. Deline, and P. F. Green, *Macromolecules* **22**, 2581 (1989); P. C. M. Grim *et al.*, *ibid.* **28**, 7501 (1995).

<sup>8</sup>G. J. Kellogg *et al.*, *Phys. Rev. Lett.* **76**, 2503 (1996).

<sup>9</sup>N. Koneripalli *et al.*, *Langmuir* **26**, 6681 (1996).

<sup>10</sup>P. Lambooy *et al.*, *Phys. Rev. Lett.* **72**, 2899 (1994); N. Koneripalli *et al.*, *Macromolecules* **28**, 2897 (1995).

<sup>11</sup>M. Kikuchi and K. Binder, *J. Chem. Phys.* **101**, 3369 (1994).

<sup>12</sup>E. Helfand, *J. Chem. Phys.* **62**, 999 (1975).

<sup>13</sup>K. R. Shull, *Macromolecules* **25**, 2122 (1992).

<sup>14</sup>A. N. Semenov, *Sov. Phys. JETP* **61**, 733 (1985).

<sup>15</sup>J. D. Vavasour and M. D. Whitmore, *Macromolecules* **26**, 7070 (1993); **29**, 5244 (1996); M. W. Matsen and M. Schick, *ibid.* **27**, 4014 (1994); M. W. Matsen and F. S. Bates, *J. Polym. Sci. Part B* (in press).

<sup>16</sup>D. T. Wu *et al.*, *J. Polym. Sci. Part B* **33**, 2373 (1995); D. T. Wu, G. H. Fredrickson, and J.-P. Carton, *J. Chem. Phys.* **104**, 6387 (1996).

<sup>17</sup>F. Schmid, *J. Chem. Phys.* **104**, 9191 (1996).

<sup>18</sup>M. W. Matsen and M. Schick, *Phys. Rev. Lett.* **72**, 2660 (1994).

<sup>19</sup>D. G. Walton *et al.*, *Macromolecules* **27**, 6225 (1994).

<sup>20</sup>M. S. Turner, *Phys. Rev. Lett.* **69**, 1788 (1992).

<sup>21</sup>I. M. Lifshitz, A. Yu. Grosberg, and A. R. Khokhlov, *Rev. Mod. Phys.* **50**, 683 (1978).

<sup>22</sup>We define the interface as the locus  $\phi_A(\mathbf{r}) = \phi_B(\mathbf{r})$  and the interfacial width as  $w = |\mathbf{n} \cdot \nabla \phi_A(\mathbf{r})|^{-1}$  evaluated at the interface, where  $\mathbf{n}$  is a unit vector normal to the interface.

<sup>23</sup>S. P. Gido and E. L. Thomas, *Macromolecules* **27**, 6137 (1994).

<sup>24</sup>N. Singh, F. S. Bates, and M. Tirrell, *Phys. Rev. Lett.* **75**, 976 (1995).

<sup>25</sup>M. W. Matsen and F. S. Bates, *Macromolecules* **28**, 8884 (1995).

<sup>26</sup>S. T. Milner and D. C. Morse, *Phys. Rev. E* **54**, 3793 (1996).

<sup>27</sup>M. S. Turner, M. Rubinstein, and C. M. Marques, *Macromolecules* **27**, 4986 (1994).

<sup>28</sup>G. Brown and A. Chakrabarti, *J. Chem. Phys.* **101**, 3310 (1994); **102**, 1440 (1995).

<sup>29</sup>M. Kikuchi and K. Binder, *Europhys. Lett.* **21**, 427 (1993).

<sup>30</sup>U. Micka and K. Binder, *Macromol. Theory Simul.* **4**, 419 (1995).

<sup>31</sup>G. T. Pickett and A. C. Balasz, *Macromolecules* (in press).

<sup>32</sup>J. M. H. M. Scheutjens and G. J. Fleer, *J. Phys. Chem.* **83**, 1619 (1979).

<sup>33</sup>M. W. Matsen, *J. Chem. Phys.* **104**, 7758 (1996).

<sup>34</sup>M. W. Matsen and M. Schick, *Macromolecules* **27**, 6761 (1994); **27**, 7157 (1994).

<sup>35</sup>M. W. Matsen, *Phys. Rev. Lett.* **74**, 4225 (1995); *Macromolecules* **28**, 5765 (1995).

<sup>36</sup>G. T. Pickett, T. A. Witten, and S. R. Nagel, *Macromolecules* **26**, 3194 (1993).

<sup>37</sup>D. A. Hajduk *et al.*, *Macromolecules* (submitted).

<sup>38</sup>S. Qi and Z.-G. Wang, *Phys. Rev. Lett.* **76**, 1679 (1996); *Phys. Rev. E* **55**, 1682 (1997).

<sup>39</sup>E. Gattiglia, A. Turturro, D. Ricci, and A. Bonfiglio, *Macromol. Rapid Commun.* **16**, 919 (1995); P. Mansky, P. Chaikin, and E. L. Thomas, *J. Mater. Sci.* **30**, 1987 (1995).